Comparison of Three Microphysics Parameterization Schemes in the WRF Model for an Extreme Rainfall Event in the Coastal Metropolitan City of Guangzhou, China

Yongjie Huang[1], Yaping Wang[2], Lulin Xue[3], Xiaolin Wei[4], Lina Zhang[5], and Huaiyu Li[6]

[1] School of Meteorology, University of Oklahoma, Norman, OK, USA

[2] Cooperative Institute for Mesoscale Meteorological Studies, University of Oklahoma, Norman, OK, USA

[3] National Center for Atmospheric Research (NCAR), Boulder, CO, USA

[4] Meteorological Bureau of Shenzhen Municipality, Shenzhen, China

[5] China Meteorological Administration Training Centre, Beijing, China

[6] Guangzhou Meteorological Observatory, Guangzhou, China

Submitted to *Atmospheric Research* on Oct 19, 2019

Revised on Jan 27, 2020

Corresponding author: Yongjie Huang (Yongjie.Huang@ou.edu)

School of Meteorology, University of Oklahoma

120 David L. Boren Blvd., Norman, OK, USA, 73072

Abstract

An extreme rainfall event in the coastal metropolitan city of Guangzhou, China is simulated by the Weather Research and Forecasting (WRF) model using three bulk microphysics schemes to explore the capability to reproduce the observed precipitation features by these schemes and their differences. The detailed comparison among the three runs in terms of radar reflectivity, precipitation, thermodynamic fields and microphysical processes are conducted. Results show that all the simulations can reproduce the two main heavy rainfall centers in Guangzhou and the first convection initiation. The accumulated precipitation in the simulation using the WSM6 scheme performs better than the others in terms of intensity and distribution compared to observations. The weaker accumulated precipitation in the second heavy rainfall center in the simulations using the Thompson and Morrison schemes result from their more dispersed precipitation distributions dominated by the cold pool intensity and distribution. The latent heating from the water vapor condensation dominates the convection initiation and storm development. The latent cooling from the rain water evaporation dominates the cold pool intensity and distribution, which influences the storm moving and subsequent convection propagation, and finally the intensity and distribution of surface precipitation. Sensitivity experiments of the latent heat confirm the dominant roles of latent heating/cooling, especially the water vapor condensation heating and rain water evaporation cooling, in the differences of the thermodynamic fields, storm development, convection propagation and surface precipitation among the three simulations.

Keywords: microphysics parameterization; WRF; extreme rainfall; latent heat

1 Introduction

There still are large uncertainties associated with the microphysics parameterization in current numerical weather prediction (NWP) (Khain et al., 2015). Spectral bin microphysics schemes (SBMs) predict the discretized particle size distribution (PSD) and allow greater PSD characteristic flexibility, which are supposed to be conceptually more realistic and more accurate than bulk microphysics schemes (BMPs) (Khain et al., 2004; Khain et al., 2015). However, Xue et al. (2017) simulated a squall-line event using three spectral bin microphysics schemes coupled into the Weather Research and Forecasting (WRF) Model, and found that different bin microphysics schemes simulated a wide spread of microphysical, thermodynamic, and dynamic characteristics of the squall line. Fan et al. (2017) performed an intercomparison study of a midlatitude mesoscale squall line using the WRF model with eight different cloud microphysics schemes (7 BMPs and 1 SBM), and indicated that there was large variability in simulated cloud and precipitation properties using different microphysics schemes, and SBM did not always outperform the others. Besides, SBMs have a high computational cost due to the prediction of discrete sizes. Therefore, BMPs are still preferred over SBMs in current NWP models (Huang and Cui, 2015; Huang et al., 2016b).

Many previous studies have demonstrated different bin or bulk microphysics schemes frequently result in large differences in the simulated storm structures and precipitation characteristics (coverage and intensity) (Li et al., 2009; Dawson et al., 2010; Morrison and Milbrandt, 2011; Van Weverberg et al., 2012; Morrison et al. 2015; Huang et al., 2016a; Fan et al., 2017; Xue et al., 2017; Han et al., 2018; Lee and Baik, 2018; Tiwari et al., 2018; Bao et al., 2019; Falk et al., 2019; Huang et al., 2019c; Johnson et al., 2019; Labriola et al., 2019; Mohan et al., 2019). Morrison and Milbrandt (2011) performed idealized three-dimensional supercell

simulations using two double-moment bulk microphysics schemes in the WRF model, and found that many of the key differences between the baseline simulations were attributed to the different approaches in treating graupel and hail. Adams-Selin et al. (2013) indicated that bow echo development and longevity was highly sensitive to the graupel parameterization of microphysics schemes in the WRF model, and faster falling graupel led to more intense cold pools. While Xue et al. (2017) found fast falling hydrometeors have less time melting and evaporating, which leads to weaker cold pool. Choi et al. (2018) demonstrated that one scheme does not work best in all simulations of eight typhoons using five microphysics schemes of the WRF model, and suggested that the hydrometeor characteristics assumed in microphysics schemes should be carefully understood to simulate precipitating clouds. Bao et al., (2019) simulated an idealized two-dimensional squall-line using three bulk microphysics schemes in the WRF model, and found that differences in the simulated squall line development were mainly attributed to the differences in the simulated population characteristics (e.g., hydrometeor size distributions) of snow, graupel and rainwater. Falk et al. (2019) simulated an idealized supercell using one bin and one double-moment bulk microphysics schemes with the Regional Atmospheric Modeling System (RAMS) to emphasize the importance of hydrometeor fall speed on the supercell evolution and the assumptions in the schemes may be more important than the scheme class itself. Bryan and Morrison (2012) demonstrated that double-moment schemes outperformed the single-moment schemes through evaluating idealized simulations of a squall line. Luo et al. (2018) simulated a hailstorm event in eastern China using multi-moment microphysics schemes and suggested that multi-moment schemes can produce more realistic hail distribution characteristics. However, some studies also show that single-moment schemes provide better precipitation estimates compared to multi-moment schemes (Parodi and Tanelli, 2010; Cassola et al., 2015; Huang et al., 2019a). It

means that microphysics schemes will have different performances in different dynamic and thermodynamic environments, and different types of storms (e.g., squall lines, supercells). It is hard to understand why microphysics schemes result in such different simulations due to too many differences among microphysics schemes, e.g., different fundamental construction of schemes, different assumptions in parameterization of the same microphysical process (Falk et al., 2019). Therefore, more intercomparison and sensitivity studies on microphysics schemes should be performed to explore the dominant factors leading to the different simulations for individual cases.

Huang et al. (2019a) simulated an extreme rainfall event in a tropical coastal city using the WRF model nested with a very large-eddy simulation (LES). They mentioned that the simulation with the WRF single-moment 6-class microphysics (WSM6) scheme (Hong and Lim, 2006) outperformed the simulations with the Thompson double-moment scheme (Thompson et al., 2008) and the Morrison double-moment scheme (Morrison et al., 2009) through comparing the simulated radar reflectivity and precipitation against observations. However, the detailed comparison was not shown in their study. Besides, most previous intercomparison studies on microphysics schemes were performed in idealized simulations of squall lines or supercells (e.g., Dawson et al., 2010; Morrison and Milbrandt, 2011; Van Weverberg et al., 2012; Xue et al., 2017; Bao et al., 2019; Falk et al., 2019; Johnson et al., 2019). Therefore, it deserves further study on the differences among simulations with the three different microphysics schemes in this tropical deep convection shown in Huang et al. (2019a). What are the main microphysical pathways to cloud hydrometeor production? What are the main different microphysical processes among these simulations? How do the main microphysical processes influence the storm development? We will try to answer these questions in this paper.

The rest of the paper is organized as follows. Section 2 describes the extreme rainfall event and the numerical sensitivity experiments on microphysics schemes. Section 3 presents the results, and section 4 gives the summary and conclusions of the study.

2 Event description, model setup and microphysics schemes

The extreme rainfall occurred over the coastal metropolitan city of Guangzhou, southern China during 6–7 May 2017. A maximum daily rainfall of 524.1 mm and a maximum hourly rainfall of 184.4 mm were recorded in this event, causing serious floods and property damage. Huang et al. (2019a and 2019b) conducted an observation analysis and a nested large-eddy simulation (LES) using WRF model to explore mechanisms associated with this extreme rainfall event. This event took place under relatively slowly evolving synoptic and mesoscale conditions over the trumpet-shaped topography of the Pearl River Delta. The counteraction between the warm, moist southerly flow and the precipitation-produced cold pool outflows repeatedly triggered new updrafts and convection cells upstream, supporting the initiation and maintenance of a long-lived (quasi-stationary) back-building mesoscale convective system (Huang et al., 2019a). The sustained and moderately slantwise strong vertical updrafts, supported by the combination of buoyancy and dynamic acceleration and the shallow weak cool pools, generated the extreme precipitation rate (Huang et al., 2019b).

Huang et al. (2019a) mentioned that, the WSM6 microphysical parameterization scheme produced better simulations compared to other double-moment microphysical parameterization schemes in this event. Therefore, it is necessary to have an in-depth understanding of the differences among the simulations using different microphysics parameterization schemes for this extreme rainfall.

In this study, we adopted the same model setups as described in Huang et al. (2019a) except for microphysics parameterization schemes. The WRF model version 3.8.1 (Skamarock et al., 2008) was configured with three one-way nested domains with horizontal resolution of 4.5, 1.5, and 0.5 km, respectively. The model was integrated from 1200 UTC 06 to 0000 UTC 07 May 2017 (12 hours), covering the intense period of rainfall over the Guangzhou city. The 0.5-km domain was set up in LES mode, that is, no planetary boundary layer (PBL) parameterization scheme was used in this domain. Observation data from surface automatic weather stations, radiosondes, and wind profilers were assimilated into the model by the four-dimensional data assimilation (FDDA, Stauffer and Seaman, 1990) method during 1200 UTC 06–0000 UTC 07 May 2017 for 4.5- and 1.5-km domains and 1200–1600 UTC 06 May 2017 for 0.5-km domain (Huang et al., 2019a). The model simulation with the single-moment WSM6 scheme (Hong and Lim, 2006) reproduced this extreme rainfall event successfully, in terms of convection initiation, propagation, and heavy rainfall amount (Huang et al., 2019a). More details of the model configuration and verification can be found in Huang et al. (2019a). The original simulation with the WSM6 scheme is referred to as the WSM6 run. There are other two advanced double-moment microphysics schemes used to compare in this study, i.e., the Thompson (Thompson et al., 2008) and Morrison (Morrison et al., 2009) microphysics schemes. The simulations using Thompson and Morrison microphysics schemes are referred to as the THOM run and MORR run hereafter, respectively. All these three schemes predict mixing ratios of five cloud species, including cloud water, cloud ice, rainwater, snow and graupel. The detailed differences among these three cloud microphysics schemes can be referred to Bao et al. (2019). The model output data in the 0.5-km domain at 10-min intervals are used for analysis in this study.

3 Results

3.1 Radar reflectivity and precipitation

The radar reflectivity and precipitation fields are examined first to investigate the overall differences among the simulations with different microphysics schemes. Figure 1 shows observed and simulated composite reflectivity at 1600, 1700, 1800, 2100, 2200 and 2300 UTC 06 May 2017. In general, the simulated composite reflectivity from the simulations with different microphysics schemes are similar to each other in terms of the intensity and coverage (Fig. 1). A convection initiated and developed in Huadu District (HD) in all the simulations, which is consistent with the observations, though the simulated convection is displaced southwestward from the observation (Figs. 1a1–d3). The processes of simulated convections growing and merging resemble the observations. The simulated convective (composite reflectivity > 35 dBZ) and stratiform (15 dBZ < composite reflectivity < 35 dBZ) coverages are consistent with the observations (Figs. 1a4–d6). There also exist some small differences among the simulations, e.g., the convection over the western Guangzhou (Figs. 1b4–d4). From the accumulated precipitation in the Guangzhou region from 1600 UTC 06 May to 0000 UTC 07 May 2017 (Fig. 2), all the simulations reproduce the two main observed rainfall centers, i.e., one in HD and the other one between HP and ZC. Both maximum observed accumulated precipitation in Region A and Region B are larger than 240 mm (Fig. 2a). In the WSM6 run (Fig. 2b), the maximum simulated accumulated precipitation in Region A is over 200 mm, and it is more than 240 mm in Region B. And the location of maximum accumulated precipitation center in Region B in the WSM6 run is very close to the observation (blue crosses in Figs. 2a and 2b). In the THOM run (Fig. 2c), both maximum accumulated precipitation in Region A and Region B are less than 160 mm. In the MORR run (Fig. 2d), the maximum accumulated precipitation in Region A can reach 160 mm but less than 200 mm, and

177 the maximum accumulated precipitation reaches 200 mm, however, the location is more northward
178 than the observation. Therefore, the accumulated precipitation of WSM6 run is more consistent
179 with observations than those of THOM and MORR runs, especially the maximum accumulated
180 precipitation center between HP and ZC in Region B. The precipitation distributions are more
181 dispersed and the maximum accumulated precipitation is weaker in THOM and MORR runs,
182 especially in THOM run. Besides, the edge of accumulated precipitation distribution extends more
183 southward in WSM6 run than those in THOM and MORR runs, indicating the convective system
184 moves faster in WSM6 run resembling the observations.

185 To investigate the differences in the precipitation evolution among the simulations in more
186 detail, Fig. 3 shows time series of area-averaged precipitation rate and water mass flux in the two
187 rainfall centers (Region A and Region B) in WSM6, THOM and MORR runs from 1500 UTC 06
188 May to 0000 UTC 07 May 2017 in 10-min intervals . The area-averaged water mass flux is defined
189 as

190 $$QFlux = \oiint_S \sum_{\mathrm{x} \in (\mathrm{v,c,r,i,s,g})} \rho Q_{\mathrm{x}} V_{\mathrm{n}} d\sigma / A + \iint_A E_{\mathrm{S}} d\sigma / A,$$

191 where S includes the six surfaces bounding the volume within the examined region, ρ is air density,
192 Q_{x} is mixing ratio of water species including water vapor (v), cloud water (c), rainwater (r), cloud
193 ice (i), snow (s) and graupel (g), V_{n} is a wind vector component normal to the surface (inward
194 direction is positive and outward direction is negative), $d\sigma$ is an area element on the surface, A is
195 the examined region area, and E_{S} is surface evaporation flux (nearly zero in this case). That is,
196 *QFlux* is the area-averaged net flux of water mass through the surfaces bounding the volume. The
197 precipitation rate in Region A is generally larger in WSM6 run than those in THOM and MORR
198 runs, particularly in period of 1810–2130 UTC 06 May 2017 (Fig. 3a). However, this relationship
199 is different in Region B (Fig. 3b). From 2020 UTC 06 May, the area-averaged precipitation rates

200 in Region B from THOM and MORR runs are generally larger than that from WSM6 run (Fig.
201 3b), while the maximum accumulated precipitation in Region B from THOM and MORR runs are
202 smaller than that from WSM6 run (Figs. 2b–d). It is mainly due to the more dispersed precipitation
203 distributions in THOM and MORR runs. The variation of precipitation rate is consistent with the
204 variation of *QFlux*, and the variation of precipitation rate is delayed slightly in the both regions
205 (Fig. 3), indicating incoming water mass quickly transforms into precipitation.

206 From the precipitation rates in Region A (Fig. 3a), they are similar among the three simulations
207 by 1800 UTC 06 May 2017, and then their differences enlarge. The difference among the model
208 configurations of the three runs is only the microphysics schemes. The microphysics schemes may
209 produce different amounts of latent heat, which will influence the atmospheric buoyancy and then
210 change model dynamics (Huang et al., 2018; Huang et al., 2019b). Therefore, the difference in
211 latent heating should dominate the differences among the three simulations. To confirm this
212 hypothesis, three new sensitivity experiments were conducted to examine the role of latent heating
213 by turning off latent heat from the microphysics schemes. The time series of area-averaged
214 precipitation rate and *QFlux* in the two regions (Region A and Region B) in the no-latent-heating
215 experiments from 1500 UTC 06 May to 0000 UTC 07 May 2017 in 10-min intervals are shown in
216 Figs. 3c and 3d. After turning off latent heating from the microphysics schemes, the precipitation
217 rates and *QFlux* in both regions from all the sensitivity experiments are almost the same in terms
218 of the intensity and variation (Figs. 3c and 3d), which confirms the latent heating dominates the
219 differences among the simulations with different microphysics schemes.

220 **3.2 Thermodynamic differences**

221 Latent heat release can influence the thermodynamic structures (equivalent potential
222 temperature) and then change atmospheric buoyancy and dynamic features (e.g., vertical motions,

223 Huang et al., 2019b). The microphysics-induced vertical motions will in turn affect the cloud
224 microphysical processes and cloud structure. To investigate the differences in thermodynamic and
225 dynamic structures among the three simulations, Fig. 4 shows height-latitude cross sections of
226 simulated equivalent potential temperature (θ_e), density potential temperature (θ_ρ) and along cross-
227 section winds in 0.5-km domain of the WSM6, THOM and MORR runs at 1800, 1900, 2200 and
228 2300 UTC 06 May 2017. The θ_ρ here is defined following Emanuel (1994) and Panosetti et al.
229 (2016). At the early stage of storm development (near HD at 1800 and 1900 UTC), the differences
230 in the thermodynamic fields mainly exist in the storm region (Figs. 4a1–c2). There is larger θ_e in
231 the upper levels within the storm region in the WSM6 run, followed by the MORR run, and the
232 weakest in the THOM run (Figs. 4a1–c2), indicating stronger buoyancy exists in the upper levels
233 in the WSM6 run. Accordingly, the vertical motion is relatively stronger in the WSM6 and MORR
234 runs than that in the THOM run. There exists obvious cold anomaly in the lower levels in the
235 WSM6 run (Figs. 4a1 and a2), indicating the stronger and deeper cold pool in the WSM6 run. At
236 the later stage of storm (near the second rainfall center at 2200 and 2300 UTC), the thermodynamic
237 fields have obvious differences among the different simulations due to the influence of the former
238 convections and cold pool distributions (Figs. 4a3–c4). The height of strong warm anomaly in the
239 upper levels is lower in the stage than the former stage. The coverages of warm anomaly ($\theta_e > 342$
240 K) are larger in upper levels in the THOM and MORR runs than that in the WSM6 run. The cold
241 pool boundary (indicated by the 300-K θ_ρ) extends more southward in the WSM6 run than those
242 in the THOM and MORR runs, indicating stronger cold pool is simulated in the WSM6 run. It is
243 corresponding to the more southward distribution of accumulated precipitation in the WSM6 run
244 (Fig. 2).

To further explore the causes of the differences in the thermodynamic fields among the simulations, vertical profiles of spatiotemporal-averaged potential temperature tendencies due to latent heating/cooling rate of condensation/evaporation (TH_LHR_{vl}), latent heating/cooling rate of deposition/sublimation (TH_LHR_{vi}), latent heating/cooling rate of freezing/melting (TH_LHR_{li}) and total latent heating/cooling rate (TH_LHRT) in Region A during 1800–1900 UTC 06 May 2017 and in Region B during 2200–2300 UTC 06 May 2017 in the WSM6, THOM and MORR runs are shown in Fig. 5. In Region A during 1800–1900 UTC 06 May 2017, TH_LHRT is obviously larger in the WSM6 (maximum is ~2.8×10^{-3} K s^{-1}) than those in the THOM (maximum is ~2.1×10^{-3} K s^{-1}) and MORR (maximum is ~2.3×10^{-3} K s^{-1}) runs in particular above the 0 °C layer (Figs. 5a, c and e), which causes the differences in θ_e in the upper levels in the three simulations shown in Figs. 4a1–c2. The total cooling tendency (TH_LHRT < 0 K s^{-1}) in the lower troposphere below 1 km is stronger in the WSM6 run (Fig. 5a), resulting in stronger cold pool in the WSM6 run than in THOM and MORR runs (Fig. 4). TH_LHR_{vl} dominates the total latent heating below ~7 km especially near the 0 °C layer in the three simulations (Figs. 5a, c and e). TH_LHR_{vi} is dominant above ~7 km in the three simulations, and relatively stronger in WSM6 and MORR runs. TH_LHR_{li} is smaller than TH_LHR_{vl} and TH_LHR_{vi} in the three simulations. The latent cooling due to TH_LHR_{li} exists from surface to the height of 0 °C in the WSM6 run, while it exists mainly from ~2 km to the height of 0 °C in THOM and MORR runs (Figs. 5a, c and e), which is associated with the ice-phase hydrometeor (especially graupel) distribution discussed below. In Region B during 2200–2300 UTC 06 May 2017, TH_LHRT is larger in THOM (maximum is ~2.6×10^{-3} K s^{-1}) and MORR (maximum is ~2.3×10^{-3} K s^{-1}) runs than that in the WSM6 (maximum is ~2.0×10^{-3} K s^{-1}) run (Figs. 5b, d and f). The height of maximum TH_LHRT dominated by TH_LHR_{vl} is lower during 2200–2300 UTC than that during 1800–1900 UTC in the

three simulations, and TH_LHR$_{vi}$ weakens meanwhile, indicating the importance of warm-rain processes during 2200–2300 UTC (Huang et al., 2019b). The specific microphysical processes causing these differences in the latent heating profiles will be investigated in the next section.

3.3 Microphysical differences

The latent heating differences among the three runs are attributed to the differences in microphysical processes. Therefore, the detailed microphysical processes in the three simulations will be compared in this section.

The distribution of cloud hydrometeors is examined first. Figure 6 shows the vertical profiles of spatiotemporal-averaged mixing ratios of cloud water (Q_c), rain water (Q_r), cloud ice (Q_i), snow (Q_s) and graupel (Q_g) in Region A during 1800–1900 UTC 06 May 2017 and in Region B during 2200–2300 UTC 06 May 2017 in the WSM6, THOM and MORR runs. In Region A during 1800–1900 UTC 06 May 2017, Q_c has two peaks in all the three runs, one above the 0 °C layer, the other below the 0 °C layer (Figs. 6a, c and e), which may be associated with the large-scale vertical motions (Fig. 4). The magnitudes of Q_c are a little larger in the WSM6 and THOM runs than that in the MORR run. The peak of Q_r can reach 0.52×10^{-3} kg kg^{-1} in the WSM6 run, ~0.50×10^{-3} kg kg^{-1} in the THOM run, while ~0.47×10^{-3} kg kg^{-1} in the MORR run. Q_r can reach 0.46×10^{-3} kg kg^{-1} near the surface in the WSM6 run, however, it is just ~0.33×10^{-3} kg kg^{-1} in the THOM and MORR runs (Figs. 6a, c and e). The differences in ice-phase hydrometeors especially snow and graupel are relatively obvious. There is much snow in the MORR run (maximum can reach 0.40×10^{-3} kg kg^{-1}), while the maxima of Q_s in the WSM6 and THOM runs are ~0.12×10^{-3} kg kg^{-1} and ~0.14×10^{-3} kg kg^{-1}, respectively (Figs. 6a, c and e). Much graupel is simulated in the WSM6 run, and the peak of Q_g can reach 0.44×10^{-3} kg kg^{-1} near the 0 °C layer (Fig. 6a). However, the amount

of graupel is much less in the THOM and MORR runs, whose maxima of mixing ratio are 0.20 × 10^{-3} kg kg^{-1} and 0.22 × 10^{-3} kg kg^{-1}, respectively (Figs. 6c and e). The magnitudes of cloud ice are relatively small in the all simulations (Figs. 6a, c and e). The ice-phase hydrometeors in the THOM and MORR runs mainly exist above the 0 °C layer (the total mixing ratio of ice-phase hydrometeors shown in Figs. 6c and e), while there are abundant ice-phase hydrometeors below the 0 °C layer (Fig. 6a), resulting in stronger latent cooling associated with melting in the lower levels (Fig. 5a). In Region B during 2200–2300 UTC 06 May 2017, the peaks of cloud water enlarge in the three runs, especially in the THOM run (maximum is ~0.28 × 10^{-3} kg kg^{-1}). Q_r near the surface decreases to ~0.38 × 10^{-3} kg kg^{-1} in the WSM6 run (Fig. 6a), while it increases to ~0.40 × 10^{-3} kg kg^{-1} in the THOM and MORR runs (Figs. 6d and f). It indicates warm-rain processes enhance during the second stage of the rainfall. All the ice-phase hydrometeors especially graupel decrease in the WSM6 run (Fig. 6b), while they don't change a lot in the THOM run (Fig. 6d). The maximum of Q_g decreases by ~0.1 × 10^{-3} kg kg^{-1}, while the peak of Q_s increases by ~0.12 × 10^{-3} kg kg^{-1} in the MORR run (Fig. 6f).

Figs. 7–9 show vertical profiles of spatiotemporal-averaged microphysical conversion rates of cloud water, rain water, cloud ice, snow and graupel in Region A during 1800–1900 UTC 06 May 2017 in the WSM6, THOM and MORR runs, respectively. In the WSM6 run, water vapor condensation is the dominant production term of cloud water, and the main sink terms of cloud water are collection by rain, collection by snow and graupel and autoconversion to rain (Fig. 7a). The main source and sink terms of cloud water in the THOM and MORR runs (Figs. 8a and 9a) are the same as those in the WSM6 run. Among the three runs, the stronger water vapor condensation in the WSM6 run (Fig. 7a) results in stronger latent heating due to TH_LHR_{vl} (Fig. 5a). The common dominant pathways for rain water production in the three runs are rain collecting

cloud water and graupel melting (Figs. 7–9b). The rainwater evaporation is the common sink term of rain water below the 0 °C layer (Figs. 7–9b), and stronger in the WSM6 run (Fig. 7b), corresponding to the stronger cold pool in the WSM6 run (Fig. 4). From the raindrop size distribution at 0.5 km in Region A during 1800–1900 UTC 06 May 2017 (Fig. 10), there are much more small raindrops in the WSM6 run, which is more favorable to evaporation. The near-surface sedimentation of rain water is stronger in the WSM6 run (Fig. 7b), followed by the MORR run (Fig. 9b), and it is the smallest in the THOM run (Fig. 8b). It is consistent with the larger surface precipitation rate in the WSM6 and MORR runs (Fig. 3a).

The source and sink terms of cloud ice are relatively larger in the WSM6 run compared to those in the THOM and MORR runs (Figs. 7–9c), corresponding to larger amount of cloud ice in the upper troposphere in the WSM6 run than the other two runs (Figs. 6a, c and e). The water vapor deposition to form cloud ice is the dominant cloud ice production term in the WSM6 run (Fig. 7c), which mainly contributes to latent heating due to TH_LHR$_{vi}$ (Fig. 5a). As for the snow, the total snow tendency in the MORR run is the largest among the three runs due to stronger collection of rain water and cloud water by snow to form snow and the relatively smaller sink terms of snow in the MORR run (Figs. 7–9d), resulting in much more snow in the MORR run than the other two runs (Figs. 6a, c and e). The common dominant snow production terms in the THOM and MORR runs are snow collecting cloud water and water vapor deposition to form snow (Figs. 8d and 9d). The water vapor deposition to form snow in these two runs mainly contributes to latent heating due to TH_LHR$_{vi}$ (Figs. 5c and e). As for the graupel production, the total graupel tendency near the 0 °C layer in the WSM6 run is the largest (mainly due to the strongest sedimentation of graupel) among the three runs (Figs. 7–9e), resulting in much more graupel in the WSM6 run than the THOM and MORR runs (Figs. 6a, c and e). The source and sink terms of graupel are mainly above

2 km in the THOM run, corresponding to the graupel distribution in the THOM run (Fig. 6c). The main graupel production terms in the WSM6 run are collection between rain and snow to form graupel, collection of cloud water by averaged snow and graupel and collection between ice and rain to form graupel (Fig. 7e). The common main graupel production term in the THOM and MORR runs is collection of cloud water by graupel (Figs. 8e and 9e). The dominant graupel consumption in the three runs is graupel melting (Figs. 7–9e).

The dominant microphysical processes in Region B during 2200–2300 UTC 06 May 2017 are the same as those in Region A during 1800–1900 UTC 06 May 2017 in the three runs, and the warm rain processes enhance and ice phase processes weaken (not shown), which is consistent with the distributions of thermodynamic fields (Figs. 4a3–c4) and cloud hydrometeors (Figs. 6b, d and f).

Therefore, latent heating due to water vapor condensation to form cloud water dominates the differences among the three runs. Rain water evaporation dominates the cold pool intensity, which influences the convection moving and propagation. To confirm these conclusions, the other two groups of sensitivity experiments are conducted. One group turns off the latent heat due to water vapor condensation to form cloud water, and the other group turns off the latent heat due to rain water evaporation. Figure 11 shows the 8-h accumulated precipitation in the 0.5-km domain of the WSM6, THOM and MORR runs after turning off latent heating due to water vapor condensation to form cloud water and rain water evaporation in the Guangzhou region from 1600 UTC 06 May to 0000 UTC 07 May 2017. After turning off latent heating from water vapor condensation, precipitation in the three runs almost disappear (Figs. 11a–c), indicating the dominant role of condensation latent heating. After turning off latent cooling from rain water evaporation, precipitation in the three runs are more concentrated and much heavier compared to the original

runs, and they are similar to each other in terms of distribution and intensity, especially between the THOM and MORR runs (Figs. 11d–f). The hydrometeor distribution and microphysical processes are similar with those in Region A in the original experiments, except larger magnitudes in the sensitivity experiments (not shown). It indicates rain water evaporation cooling dominates the cold pool intensity, and then influences the convection moving and propagation, and finally affects the intensity and distribution of surface precipitation.

4 Summary and conclusions

In this study, three bulk microphysics schemes in the Weather Research and Forecasting (WRF) model, the single moment WSM6 scheme and advanced double moment Thompson and Morrison schemes, are selected to simulate an extreme rainfall event in the coastal metropolitan city of Guangzhou, China during 6–7 May 2017. The detailed comparison in terms of radar reflectivity, precipitation, thermodynamic fields and microphysical processes are conducted to investigate how microphysics scheme influences the heavy rainfall among the three runs. The major findings are summarized as follows.

(1) All simulations can reproduce the convection initiation in HD and the two main heavy rainfall centers in Guangzhou, which are consistent with the observations during this extreme rainfall event. However, the accumulated precipitation in the simulation using WSM6 scheme resembles the observations in terms of intensity and distribution better. The simulation using WSM6 scheme can produce both stronger accumulated precipitation and precipitation rate in the first heavy rainfall center in HD, and it produces stronger accumulated precipitation though the precipitation rate is relatively weaker in the second heavy rainfall center compared to the simulations using the Thompson and Morrison schemes which have more dispersed precipitation distributions.

(2) The differences in latent heating from the different microphysics schemes dominate the differences in the thermodynamic fields, storm development and surface precipitation among the three simulations. After turning off latent heating from the microphysics schemes, the precipitation rates and water mass fluxes in both heavy rainfall regions significantly reduce (precipitation rates are close to zero) and are almost the same in terms of the intensity and variation in the three sensitivity experiments.

(3) Much more graupel is simulated in the simulation using the WSM6 scheme, while much more snow is simulated in the simulation using the Morrison scheme. The latent heating from the water vapor condensation is dominant in all the three simulations, and its differences lead to different convection development. Stronger latent cooling from the rain water evaporation in the low troposphere in the simulation using the WSM6 scheme generates stronger cold pool, which influences convection moving and subsequent propagation, and finally the intensity and distribution of surface precipitation. It answers why less amount of rain water, weaker latent heating, and smaller precipitation rate are simulated in the second heavy rainfall center in the simulation using the WSM6 scheme, while finally larger accumulated precipitation is produced in this simulation.

These results demonstrate the importance of the warm-rain processes including the water vapor condensation and rain water evaporation in this extreme rainfall event. The latent heating from the water vapor condensation dominates the convection initiation and storm development. The latent cooling from the rain water evaporation dominates the cold pool intensity, which influences the storm moving and subsequent convection propagation. The different simulation results using different microphysics schemes mainly result from the differences in these two processes. And the differences in these microphysical processes may be attributed to different rain water production,

405 drop size distributions, conversion rate parameterizations, etc. Therefore, how to improve the
406 expression of these processes in the model in the simulation and forecast of tropical convection
407 requires more attention in future.

408 ***Acknowledgments***

409 This work was partially supported by the National Key R&D Program of China
410 (2018YFC1507606) and the National Natural Science Foundation of China (41705031). Part
411 of this work was supported by the National Center of Meteorology, Abu Dhabi, UAE under the
412 UAE Research Program for Rain Enhancement Science. The authors appreciate editor and two
413 anonymous reviewers for their comments that contribute to improving the manuscript. The data
414 used in this study can be download online (through https://pan.baidu.com/s/1Hh8gSXpmPZ1UE8-
415 n06-e7g). The authors acknowledge high-performance computing support from Cheyenne
416 (doi:10.5065/D6RX99HX) provided by NCAR's Computational and Information Systems
417 Laboratory, sponsored by the National Science Foundation. NCAR is sponsored by the National
418 Science Foundation.

References

Adams-Selin, R.D., van den Heever, S.C., Johnson, R.H., 2013. Impact of Graupel Parameterization Schemes on Idealized Bow Echo Simulations. Monthly Weather Review 141, 1241–1262. https://doi.org/10.1175/MWR-D-12-00064.1

Bao, J.-W., Michelson, S.A., Grell, E.D., 2019. Microphysical Process Comparison of Three Microphysics Parameterization Schemes in the WRF Model for an Idealized Squall-Line Case Study. Monthly Weather Review 147, 3093–3120. https://doi.org/10.1175/MWR-D-18-0249.1

Bryan, G.H., Morrison, H., 2012. Sensitivity of a Simulated Squall Line to Horizontal Resolution and Parameterization of Microphysics. Monthly Weather Review 140, 202–225. https://doi.org/10.1175/MWR-D-11-00046.1

Cassola, F., Ferrari, F., Mazzino, A., 2015. Numerical simulations of Mediterranean heavy precipitation events with the WRF model: A verification exercise using different approaches. Atmospheric Research 164–165, 210–225. https://doi.org/10.1016/j.atmosres.2015.05.010

Choi, Y., Shin, D.-B., Joh, M., 2018. Assessment of WRF microphysics schemes in simulation of extreme precipitation events based on microwave radiative signatures. International Journal of Remote Sensing 39, 8527–8551. https://doi.org/10.1080/01431161.2018.1488288

Dawson, D.T., Xue, M., Milbrandt, J.A., Yau, M.K., 2010. Comparison of Evaporation and Cold Pool Development between Single-Moment and Multimoment Bulk Microphysics Schemes in Idealized Simulations of Tornadic Thunderstorms. Monthly Weather Review 138, 1152–1171. https://doi.org/10.1175/2009MWR2956.1

Emanuel, K.A., 1994. Atmospheric convection. Oxford University Press on Demand.

441 Falk, N.M., Igel, A.L., Igel, M.R., 2019. The Relative Impact of Ice Fall Speeds and Microphysics
442 Parameterization Complexity on Supercell Evolution. Monthly Weather Review 147, 2403–
443 2415. https://doi.org/10.1175/MWR-D-18-0417.1
444 Fan, J., Han, B., Varble, A., Morrison, H., North, K., Kollias, P., Chen, B., Dong, X., Giangrande,
445 S.E., Khain, A., Lin, Y., Mansell, E., Milbrandt, J.A., Stenz, R., Thompson, G., Wang, Y.,
446 2017. Cloud-resolving model intercomparison of an MC3E squall line case: Part I—
447 Convective updrafts. Journal of Geophysical Research: Atmospheres 122, 9351–9378.
448 https://doi.org/10.1002/2017JD026622
449 Han, M., Braun, S.A., Matsui, T., Iguchi, T., 2018. Comparisons of bin and bulk microphysics
450 schemes in simulations of topographic winter precipitation with radar and radiometer
451 measurements. Quarterly Journal of the Royal Meteorological Society 144, 1926–1946.
452 https://doi.org/10.1002/qj.3393
453 Hong, S.-Y., Lim, J.-O.J., 2006. The WRF single-moment 6-class microphysics scheme (WSM6).
454 Journal of the Korean Meteorological Society 42, 129–151.
455 Huang, Y., Cui, X., 2015. Dominant cloud microphysical processes of a torrential rainfall event in
456 Sichuan, China. Advances in Atmospheric Sciences 32, 389–400.
457 https://doi.org/10.1007/s00376-014-4066-7
458 Huang, Y., Cui, X., Li, X., 2016a. A three-dimensional WRF-based precipitation equation and its
459 application in the analysis of roles of surface evaporation in a torrential rainfall event.
460 Atmospheric Research 169, 54–64. https://doi.org/10.1016/j.atmosres.2015.09.026
461 Huang, Y., Cui, X., Wang, Y., 2016b. Cloud microphysical differences with precipitation intensity
462 in a torrential rainfall event in Sichuan, China. Atmospheric and Oceanic Science Letters 9,
463 90–98. https://doi.org/10.1080/16742834.2016.1139436

Huang, Y., Liu, Yubao, Liu, Yuewei, Li, H., Knievel, J.C., 2019a. Mechanisms for a Record-Breaking Rainfall in the Coastal Metropolitan City of Guangzhou, China: Observation Analysis and Nested Very Large Eddy Simulation With the WRF Model. Journal of Geophysical Research: Atmospheres 124, 1370–1391. https://doi.org/10.1029/2018JD029668

Huang, Y., Liu, Yubao, Liu, Yuewei, Knievel, J.C., 2019b. Budget Analyses of a Record-Breaking Rainfall Event in the Coastal Metropolitan City of Guangzhou, China. Journal of Geophysical Research: Atmospheres. https://doi.org/10.1029/2018JD030229

Huang, Y., Liu, Yubao, Xu, M., Liu, Yuewei, Pan, L., Wang, H., Cheng, W.Y.Y., Jiang, Y., Lan, H., Yang, H., Wei, X., Zong, R., Cao, C., 2018. Forecasting severe convective storms with WRF-based RTFDDA radar data assimilation in Guangdong, China. Atmospheric Research 209, 131–143. https://doi.org/10.1016/j.atmosres.2018.03.010

Huang, Y., Wang, Y., Cui, X., 2019c. Differences between Convective and Stratiform Precipitation Budgets in a Torrential Rainfall Event. Advances in Atmospheric Sciences 36, 495–509. https://doi.org/10.1007/s00376-019-8159-1

Johnson, M., Jung, Y., Milbrandt, J.A., Morrison, H., Xue, M., 2019. Effects of the Representation of Rimed Ice in Bulk Microphysics Schemes on Polarimetric Signatures. Monthly Weather Review. https://doi.org/10.1175/MWR-D-18-0398.1

Khain, A., Pokrovsky, A., Pinsky, M., Seifert, A., Phillips, V., 2004. Simulation of Effects of Atmospheric Aerosols on Deep Turbulent Convective Clouds Using a Spectral Microphysics Mixed-Phase Cumulus Cloud Model. Part I: Model Description and Possible Applications. Journal of the Atmospheric Sciences 61, 2963–2982. https://doi.org/10.1175/JAS-3350.1

Khain, A.P., Beheng, K.D., Heymsfield, A., Korolev, A., Krichak, S.O., Levin, Z., Pinsky, M., Phillips, V., Prabhakaran, T., Teller, A., van den Heever, S.C., Yano, J.-I., 2015. Representation of microphysical processes in cloud-resolving models: Spectral (bin) microphysics versus bulk parameterization: BIN VS BULK. Reviews of Geophysics 53, 247–322. https://doi.org/10.1002/2014RG000468

Labriola, J., Snook, N., Xue, M., Thomas, K.W., 2019. Forecasting the 8 May 2017 Severe Hail Storm in Denver, Colorado, at a Convection-Allowing Resolution: Understanding Rimed Ice Treatments in Multimoment Microphysics Schemes and Their Effects on Hail Size Forecasts. Monthly Weather Review 147, 3045–3068. https://doi.org/10.1175/MWR-D-18-0319.1

Lee, H., Baik, J.-J., 2018. A Comparative Study of Bin and Bulk Cloud Microphysics Schemes in Simulating a Heavy Precipitation Case. Atmosphere 9, 475. https://doi.org/10.3390/atmos9120475

Li, X., Tao, W.-K., Khain, A.P., Simpson, J., Johnson, D.E., 2009. Sensitivity of a Cloud-Resolving Model to Bulk and Explicit Bin Microphysical Schemes. Part I: Comparisons. Journal of the Atmospheric Sciences 66, 3–21. https://doi.org/10.1175/2008JAS2646.1

Luo, L., Xue, M., Zhu, K., Zhou, B., 2018. Explicit Prediction of Hail in a Long-Lasting Multicellular Convective System in Eastern China Using Multimoment Microphysics Schemes. Journal of the Atmospheric Sciences 75, 3115–3137. https://doi.org/10.1175/JAS-D-17-0302.1

Mohan, P.R., Srinivas, C.V., Yesubabu, V., Baskaran, R., Venkatraman, B., 2019. Tropical cyclone simulations over Bay of Bengal with ARW model: Sensitivity to cloud microphysics schemes. Atmospheric Research 230, 104651. https://doi.org/10.1016/j.atmosres.2019.104651

509 Morrison, H., Milbrandt, J., 2011. Comparison of Two-Moment Bulk Microphysics Schemes in
510 Idealized Supercell Thunderstorm Simulations. Monthly Weather Review 139, 1103–1130.
511 https://doi.org/10.1175/2010MWR3433.1
512 Morrison, H., Milbrandt, J.A., Bryan, G.H., Ikeda, K., Tessendorf, S.A., Thompson, G., 2015.
513 Parameterization of Cloud Microphysics Based on the Prediction of Bulk Ice Particle
514 Properties. Part II: Case Study Comparisons with Observations and Other Schemes. Journal
515 of the Atmospheric Sciences 72, 312–339. https://doi.org/10.1175/JAS-D-14-0066.1
516 Morrison, H., Thompson, G., Tatarskii, V., 2009. Impact of Cloud Microphysics on the
517 Development of Trailing Stratiform Precipitation in a Simulated Squall Line: Comparison of
518 One- and Two-Moment Schemes. Monthly Weather Review 137, 991–1007.
519 https://doi.org/10.1175/2008MWR2556.1
520 Panosetti, D., Böing, S., Schlemmer, L., Schmidli, J., 2016. Idealized Large-Eddy and Convection-
521 Resolving Simulations of Moist Convection over Mountainous Terrain. Journal of the
522 Atmospheric Sciences 73, 4021–4041. https://doi.org/10.1175/JAS-D-15-0341.1
523 Parodi, A., Tanelli, S., 2010. Influence of turbulence parameterizations on high-resolution
524 numerical modeling of tropical convection observed during the TC4 field campaign. Journal
525 of Geophysical Research 115. https://doi.org/10.1029/2009JD013302
526 Skamarock, W.C., Klemp, J.B., Dudhia, J., Gill, D.O., Barker, D.M., Wang, W., Powers, J.G.,
527 2008. A description of the Advanced Research WRF version 3. NCAR Technical note-475+
528 STR.
529 Stauffer, D.R., Seaman, N.L., 1990. Use of four-dimensional data assimilation in a limited area
530 mesoscale model. Part I: experiments with synoptic-scale data. Monthly Weather Review 118
531 (6), 1250–1277.

532 Thompson, G., Field, P.R., Rasmussen, R.M., Hall, W.D., 2008. Explicit Forecasts of Winter
533 Precipitation Using an Improved Bulk Microphysics Scheme. Part II: Implementation of a
534 New Snow Parameterization. Monthly Weather Review 136, 5095–5115.
535 https://doi.org/10.1175/2008MWR2387.1
536 Tiwari, S., Kar, S.C., Bhatla, R., 2018. Dynamic downscaling over western Himalayas: Impact of
537 cloud microphysics schemes. Atmospheric Research 201, 1–16.
538 https://doi.org/10.1016/j.atmosres.2017.10.007
539 Van Weverberg, K., Vogelmann, A.M., Morrison, H., Milbrandt, J.A., 2012. Sensitivity of
540 Idealized Squall-Line Simulations to the Level of Complexity Used in Two-Moment Bulk
541 Microphysics Schemes. Monthly Weather Review 140, 1883–1907.
542 https://doi.org/10.1175/MWR-D-11-00120.1
543 Xue, L., Fan, J., Lebo, Z.J., Wu, W., Morrison, H., Grabowski, W.W., Chu, X., Geresdi, I., North,
544 K., Stenz, R., Gao, Y., Lou, X., Bansemer, A., Heymsfield, A.J., McFarquhar, G.M.,
545 Rasmussen, R.M., 2017. Idealized Simulations of a Squall Line from the MC3E Field
546 Campaign Applying Three Bin Microphysics Schemes: Dynamic and Thermodynamic
547 Structure. Monthly Weather Review 145, 4789–4812. https://doi.org/10.1175/MWR-D-16-
548 0385.1
549

550 **Figure captions**

551 **Fig. 1.** (a1–a6) Observed and (b1–b6: WSM6 run; c1–c6: THOM run; d1–d6: MORR run)
552 simulated (in 0.5-km domain) composite radar reflectivity (dBZ) over the Guangzhou region at
553 1600, 1700, 1800, 2100, 2200 and 2300 UTC 06 May 2017, respectively. The solid black lines
554 represent Guangzhou City and its district borders. Tick marks are included every 50 km. The
555 initials in (b1) are as follows: HD = Huadu District; CH = Conghua District; BY = Baiyun District;
556 HP = Huangpu District; ZC = Zengcheng District; PY = Panyu District; NS = Nansha District. The
557 dashed magenta rectangles represent the position of cross sections shown in Fig. 4.

558 **Fig. 2.** Accumulated precipitation (mm) in the (a) observation, (b) 0.5-km domain of WSM6 run,
559 (c) THOM run and (d) MORR run in the Guangzhou region from 1600 UTC 06 May to 0000 UTC
560 07 May 2017. The blue crosses indicate the center of maximum accumulated precipitation in the
561 observations. The black solid lines represent Guangzhou City and its district borders. The initials
562 are the same as those in Fig. 1. Tick marks are included every 50 km. The dashed magenta
563 rectangles represent the regions for average precipitation shown in Fig. 3.

564 **Fig. 3.** Time series of area-averaged precipitation rate (solid thick lines, mm h^{-1}) and water mass
565 flux (circle-thin lines, mm h^{-1}) in (a) Region A and (b) Region B in 0.5-km domain of WSM6
566 (red), THOM (blue) and MORR (black) runs from 1500 UTC 06 May to 0000 UTC 07 May 2017
567 in 10-min intervals. (c) as (a) and (d) as (b), but for the experiments turning off latent heat from
568 the microphysics schemes.

569 **Fig. 4.** Height-latitude cross section of zonal-mean simulated equivalent potential temperature
570 (color shaded in K), 300-K density potential temperature (solid black lines), along cross-section
571 winds (vertical velocity amplified by a factor of 5) in 0.5-km domain of (a1–a4) WSM6 run, (b1–

572 b4) THOM run and (c1–c4) MORR run at (a1, b1, and c1) 1800, (a2, b2, and c2) 1900, (a3, b3,
573 and c3) 2200, and (a4, b4, and c4) 2300 UTC 06 May 2017.

574 **Fig. 5.** Vertical profiles of spatiotemporal-averaged potential temperature tendencies (10^{-3} K s^{-1})
575 due to latent heating/cooling rate of condensation/evaporation (red lines, TH_LHR_{vl}), latent
576 heating/cooling rate of deposition/sublimation (blue lines, TH_LHR_{vi}), latent heating/cooling rate
577 of freezing/melting (green lines, TH_LHR_{li}) and total latent heating/cooling rate (black lines,
578 TH_LHRT) in (a, c, e) Region A during 1800–1900 UTC 06 May 2017 and in (b, d, f) Region B
579 during 2200–2300 UTC 06 May 2017 in the (a, b) WSM6, (c, d) THOM and (e, f) MORR runs.
580 The horizontal dashed lines represent the height of 0 °C, and the vertical dashed lines represent 0
581 K s^{-1}.

582 **Fig. 6.** Vertical profiles of spatiotemporal-averaged mixing ratios (10^{-3} kg kg^{-1}) of cloud water
583 (blue lines, Q_c), rain water (red lines, Q_r), cloud ice (black lines, Q_i), snow (orange lines, Q_s),
584 graupel (green lines, Q_g) and sum of ice-phase hydrometeors ($Q_i + Q_s + Q_g$, black dashed lines) in
585 (a, c, e) Region A during 1800–1900 UTC 06 May 2017 and in (b, d, f) Region B during 2200–
586 2300 UTC 06 May 2017 in the (a, b) WSM6, (c, d) THOM and (e, f) MORR runs. The horizontal
587 dashed lines represent the height of 0 °C.

588 **Fig. 7.** Vertical profiles of spatiotemporal-averaged microphysical conversion rates (10^{-6} kg kg^{-1}
589 s^{-1}) of (a) cloud water (C), (b) rain water (R), (c) cloud ice (I), (d) snow (S) and (e) graupel (G) in
590 Region A during 1800–1900 UTC 06 May 2017 in the WSM6 run. The total microphysics
591 tendencies of cloud water (QCTEND), rain water (QRTEND), cloud ice (QITEND), snow
592 (QSTEND) and graupel (QGTEND) are shown by black solid curves. The horizontal dashed lines
593 represent the height of 0 °C.

594 **Fig. 8.** As in Fig. 7, but for the THOM run.

Fig. 9. As in Fig. 7, but for the MORR run.

Fig. 10. Raindrop size distribution at 0.5 km in Region A during 1800–1900 UTC 06 May 2017 in the WSM6 (blue), THOM (red) and MORR (black) runs.

Fig. 11. Accumulated precipitation (mm) in the 0.5-km domain of (a, d) WSM6 run, (b, e) THOM run and (c, f) MORR run after turning off latent heat due to (a–c) water vapor condensation to form cloud water and (d–f) rain water evaporation in the Guangzhou region from 1600 UTC 06 May to 0000 UTC 07 May 2017. The black solid lines represent Guangzhou City and its district borders. The initials are the same as those in Fig. 1. Tick marks are included every 50 km.

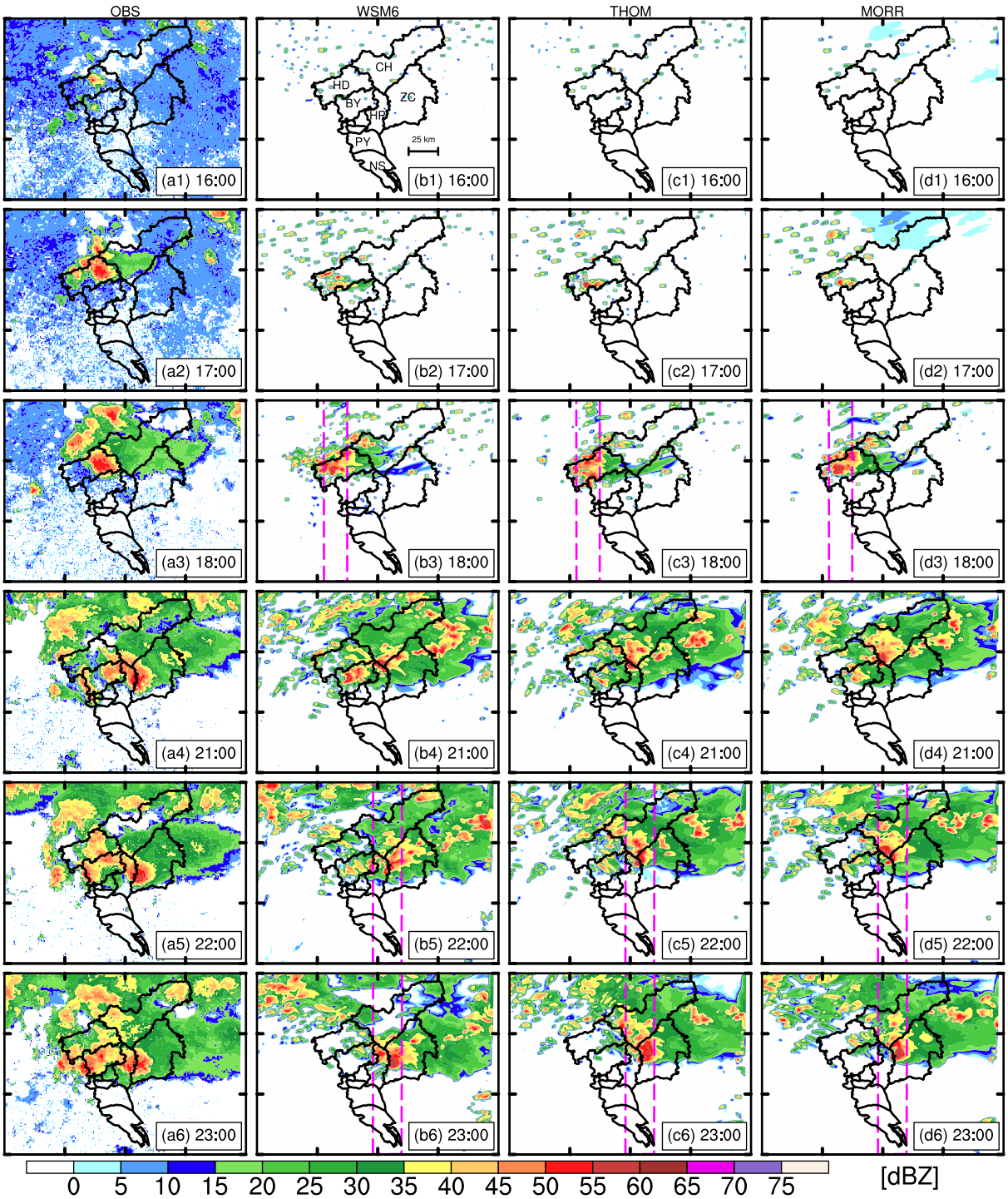

Fig. 1. (a1–a6) Observed and (b1–b6: WSM6 run; c1–c6: THOM run; d1–d6: MORR run) simulated (in 0.5-km domain) composite radar reflectivity (dBZ) over the Guangzhou region at 1600, 1700, 1800, 2100, 2200 and 2300 UTC 06 May 2017, respectively. The solid black lines represent Guangzhou City and its district borders. Tick marks are included every 50 km. The

610 initials in (b1) are as follows: HD = Huadu District; CH = Conghua District; BY = Baiyun District;
611 HP = Huangpu District; ZC = Zengcheng District; PY = Panyu District; NS = Nansha District. The
612 dashed magenta rectangles represent the position of cross sections shown in Fig. 4.
613

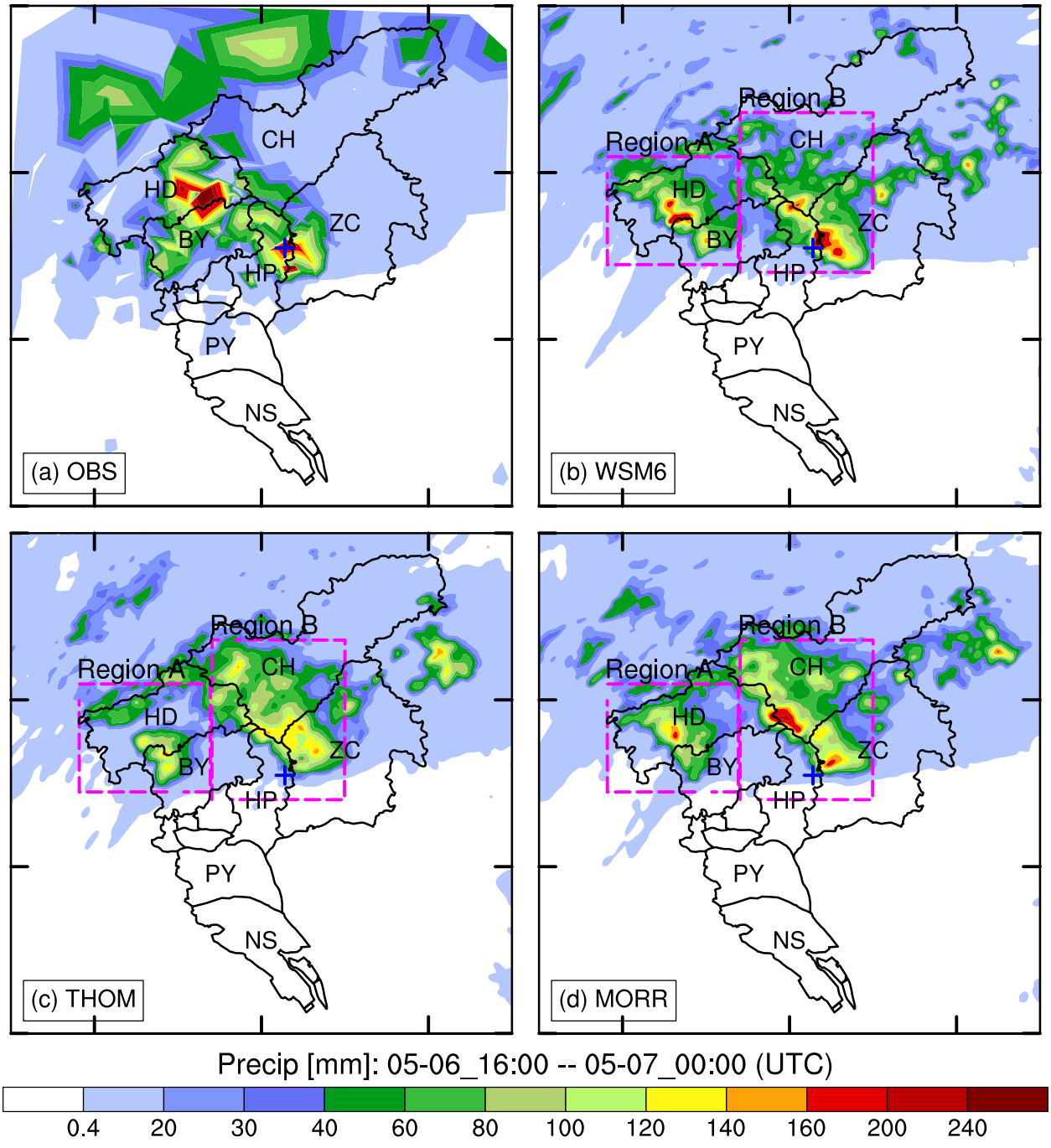

614

615 **Fig. 2.** Accumulated precipitation (mm) in the (a) observation, (b) 0.5-km domain of WSM6 run,

616 (c) THOM run and (d) MORR run in the Guangzhou region from 1600 UTC 06 May to 0000 UTC

617 07 May 2017. The blue crosses indicate the center of maximum accumulated precipitation in the

618 observations. The black solid lines represent Guangzhou City and its district borders. The initials

619 are the same as those in Fig. 1. Tick marks are included every 50 km. The dashed magenta
620 rectangles represent the regions for average precipitation shown in Fig. 3.
621

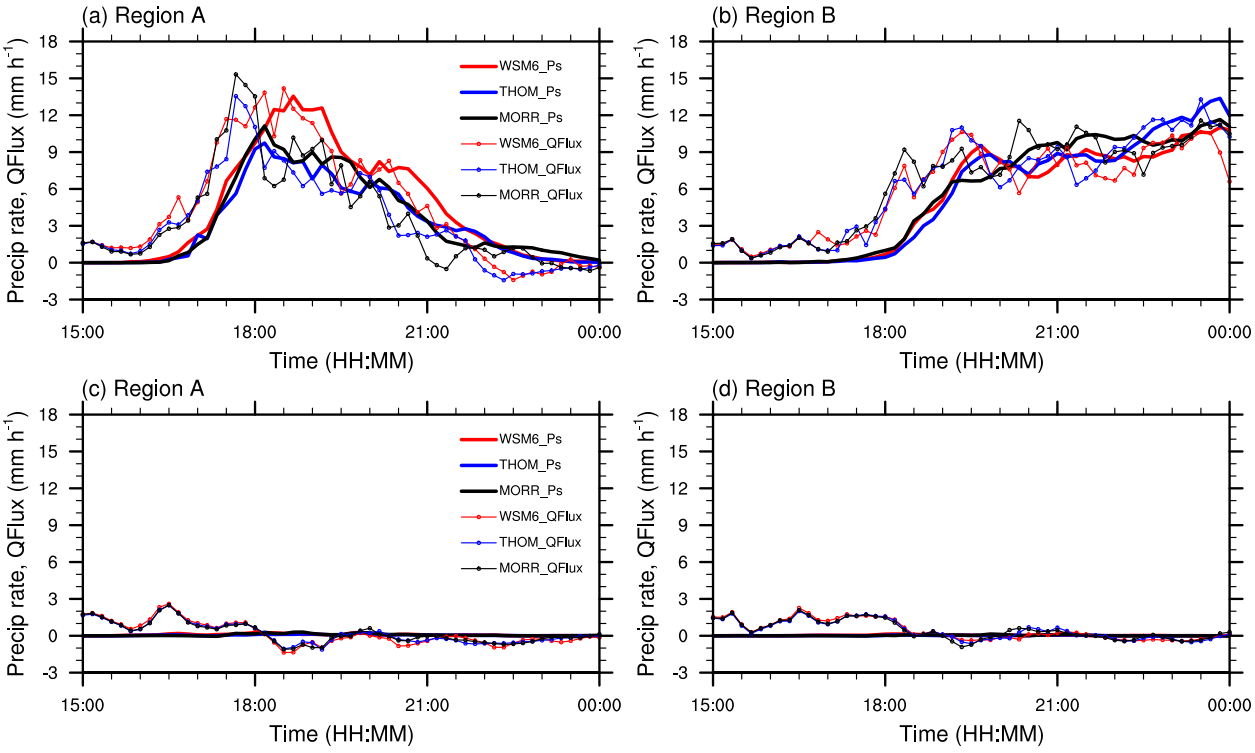

Fig. 3. Time series of area-averaged precipitation rate (solid thick lines, mm h^{-1}) and water mass flux (circle-thin lines, mm h^{-1}) in (a) Region A and (b) Region B in 0.5-km domain of WSM6 (red), THOM (blue) and MORR (black) runs from 1500 UTC 06 May to 0000 UTC 07 May 2017 in 10-min intervals. (c) as (a) and (d) as (b), but for the experiments turning off latent heat from the microphysics schemes.

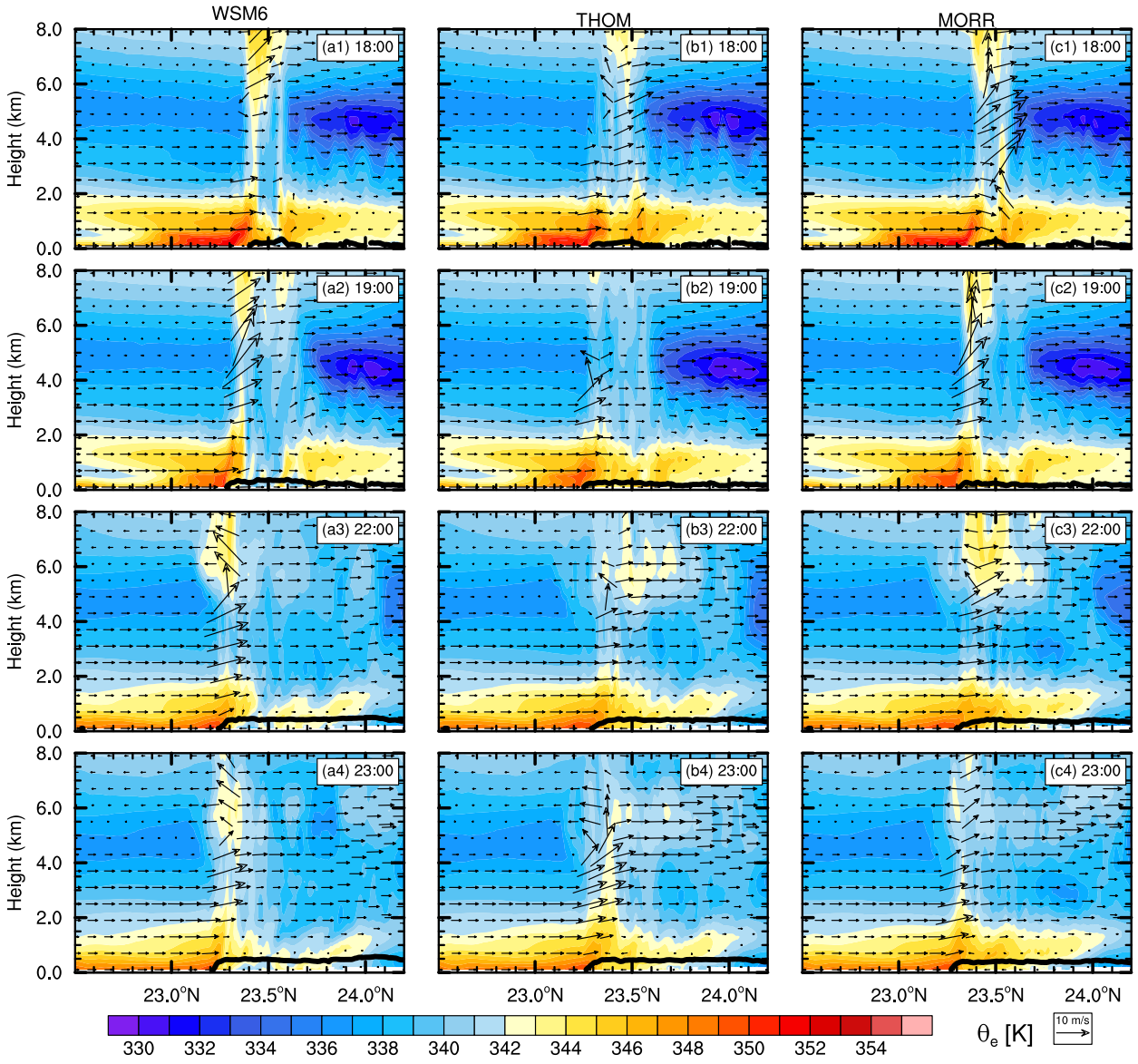

Fig. 4. Height-latitude cross section of zonal-mean simulated equivalent potential temperature (color shaded in K), 300-K density potential temperature (solid black lines), along cross-section winds (vertical velocity amplified by a factor of 5) in 0.5-km domain of (a1–a4) WSM6 run, (b1–b4) THOM run and (c1–c4) MORR run at (a1, b1, and c1) 1800, (a2, b2, and c2) 1900, (a3, b3, and c3) 2200, and (a4, b4, and c4) 2300 UTC 06 May 2017.

638

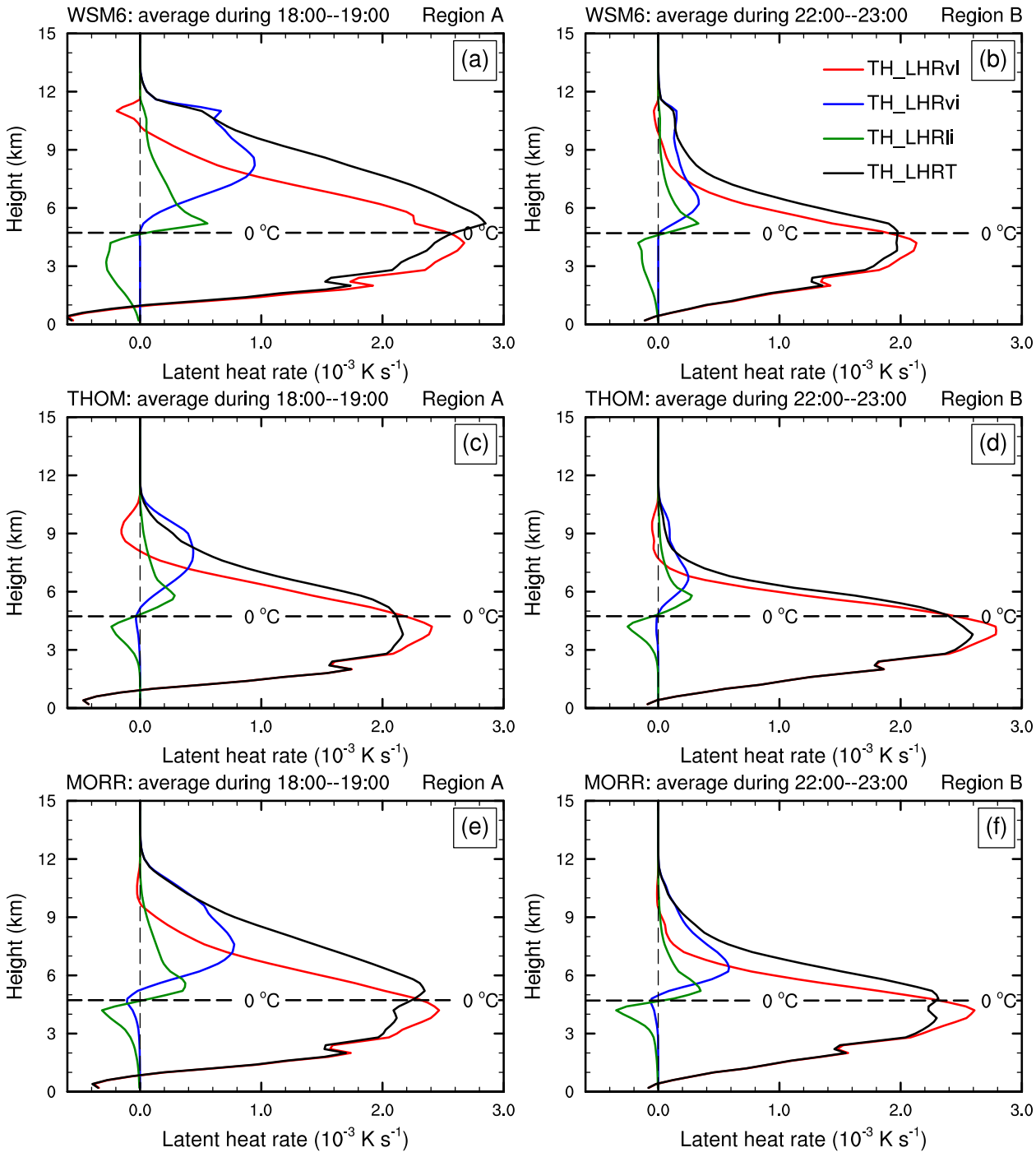

639

640 **Fig. 5.** Vertical profiles of spatiotemporal-averaged potential temperature tendencies (10^{-3} K s^{-1})
641 due to latent heating/cooling rate of condensation/evaporation (red lines, TH_LHR_{vl}), latent
642 heating/cooling rate of deposition/sublimation (blue lines, TH_LHR_{vi}), latent heating/cooling rate

643 of freezing/melting (green lines, TH_LHR_{li}) and total latent heating/cooling rate (black lines,
644 TH_LHRT) in (a, c, e) Region A during 1800–1900 UTC 06 May 2017 and in (b, d, f) Region B
645 during 2200–2300 UTC 06 May 2017 in the (a, b) WSM6, (c, d) THOM and (e, f) MORR runs.
646 The horizontal dashed lines represent the height of 0 °C, and the vertical dashed lines represent 0
647 $K\ s^{-1}$.
648

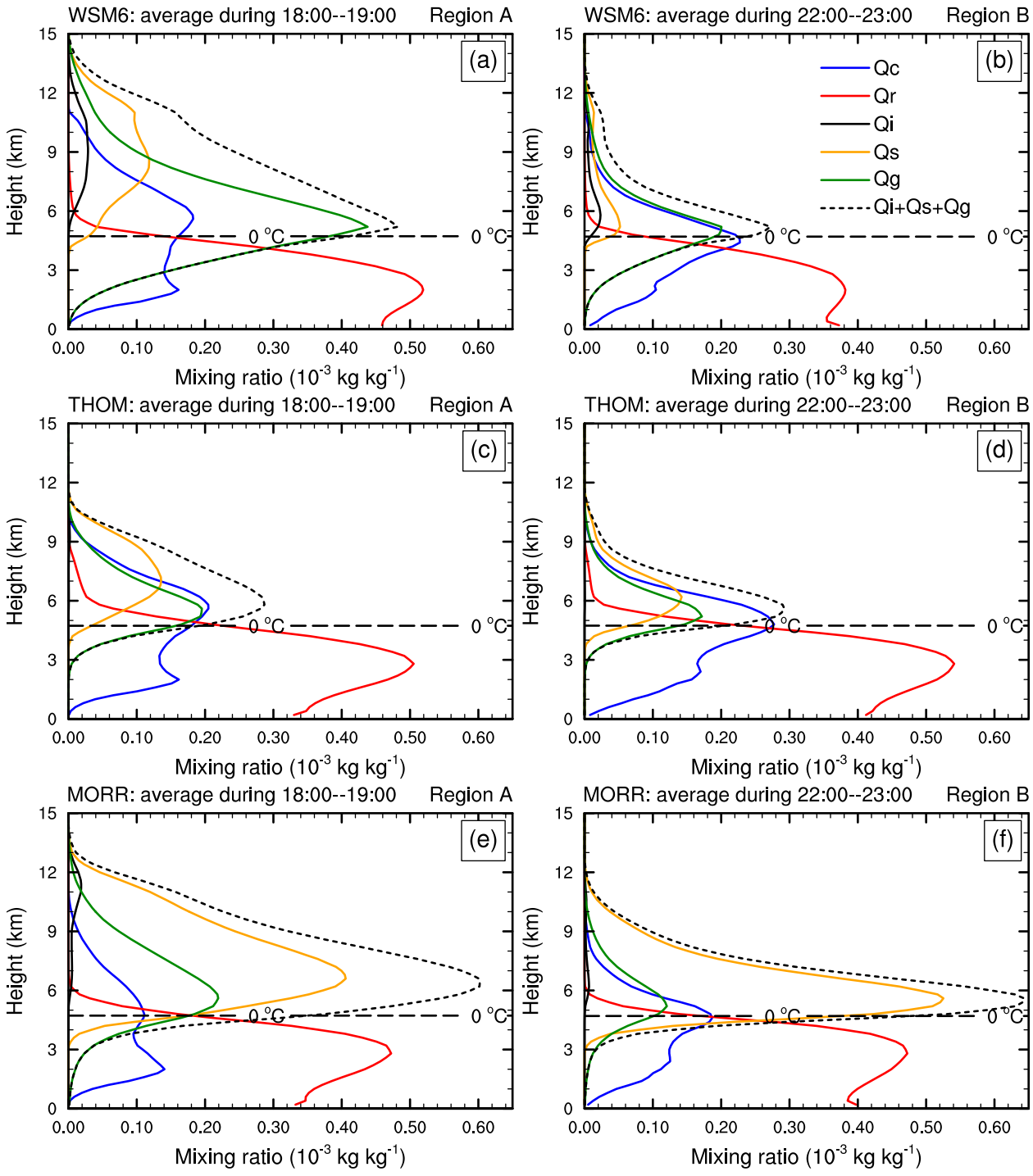

Fig. 6. Vertical profiles of spatiotemporal-averaged mixing ratios (10^{-3} kg kg^{-1}) of cloud water (blue lines, Q_c), rain water (red lines, Q_r), cloud ice (black lines, Q_i), snow (orange lines, Q_s), graupel (green lines, Q_g) and sum of ice-phase hydrometeors ($Q_i + Q_s + Q_g$, black dashed lines) in

(a, c, e) Region A during 1800–1900 UTC 06 May 2017 and in (b, d, f) Region B during 2200–2300 UTC 06 May 2017 in the (a, b) WSM6, (c, d) THOM and (e, f) MORR runs. The horizontal dashed lines represent the height of 0 °C.

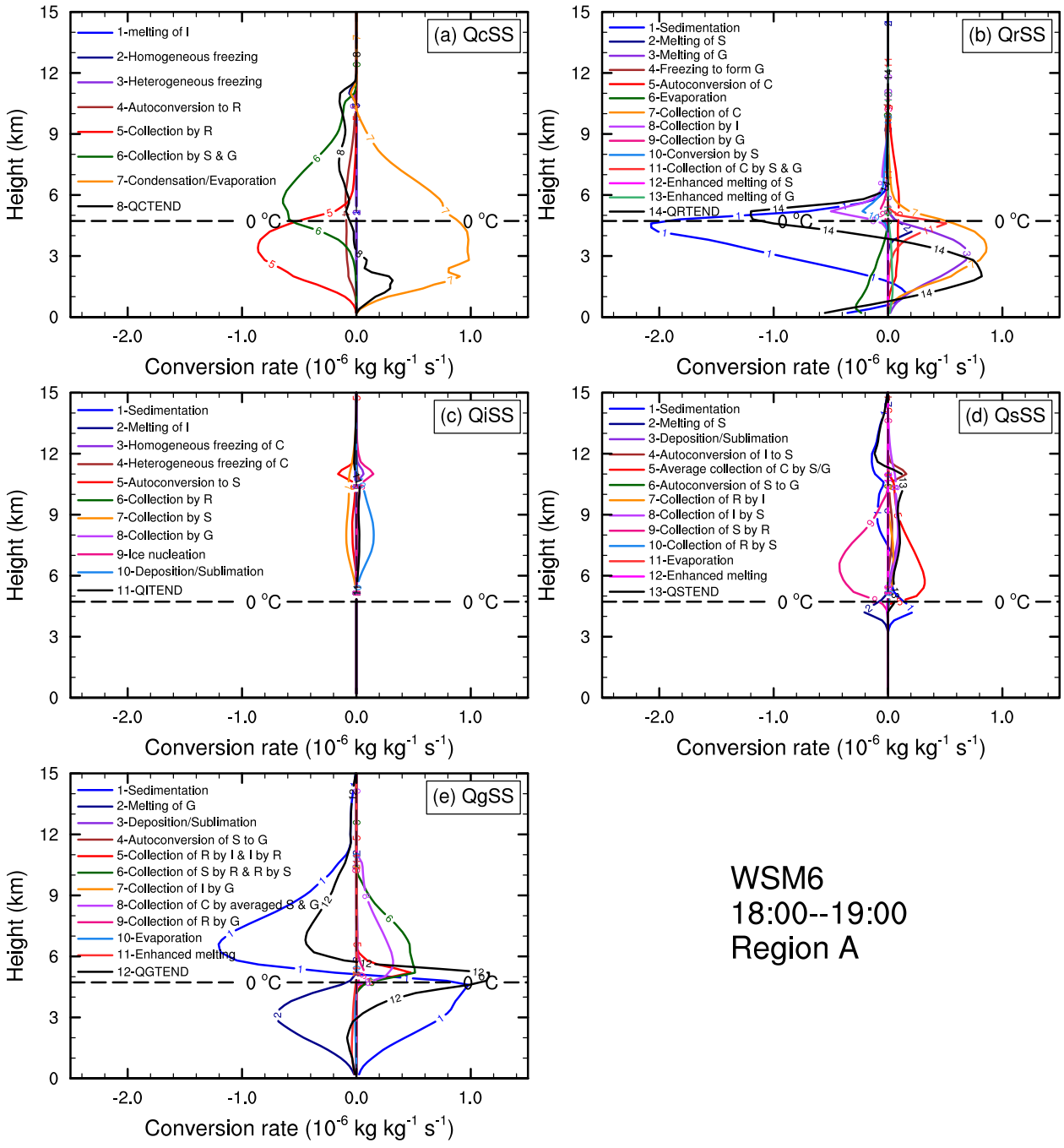

Fig. 7. Vertical profiles of spatiotemporal-averaged microphysical conversion rates (10^{-6} kg kg^{-1} s^{-1}) of (a) cloud water (C), (b) rain water (R), (c) cloud ice (I), (d) snow (S) and (e) graupel (G) in Region A during 1800–1900 UTC 06 May 2017 in the WSM6 run. The total microphysics tendencies of cloud water (QCTEND), rain water (QRTEND), cloud ice (QITEND), snow

(QSTEND) and graupel (QGTEND) are shown by black solid curves. The horizontal dashed lines represent the height of 0 °C.

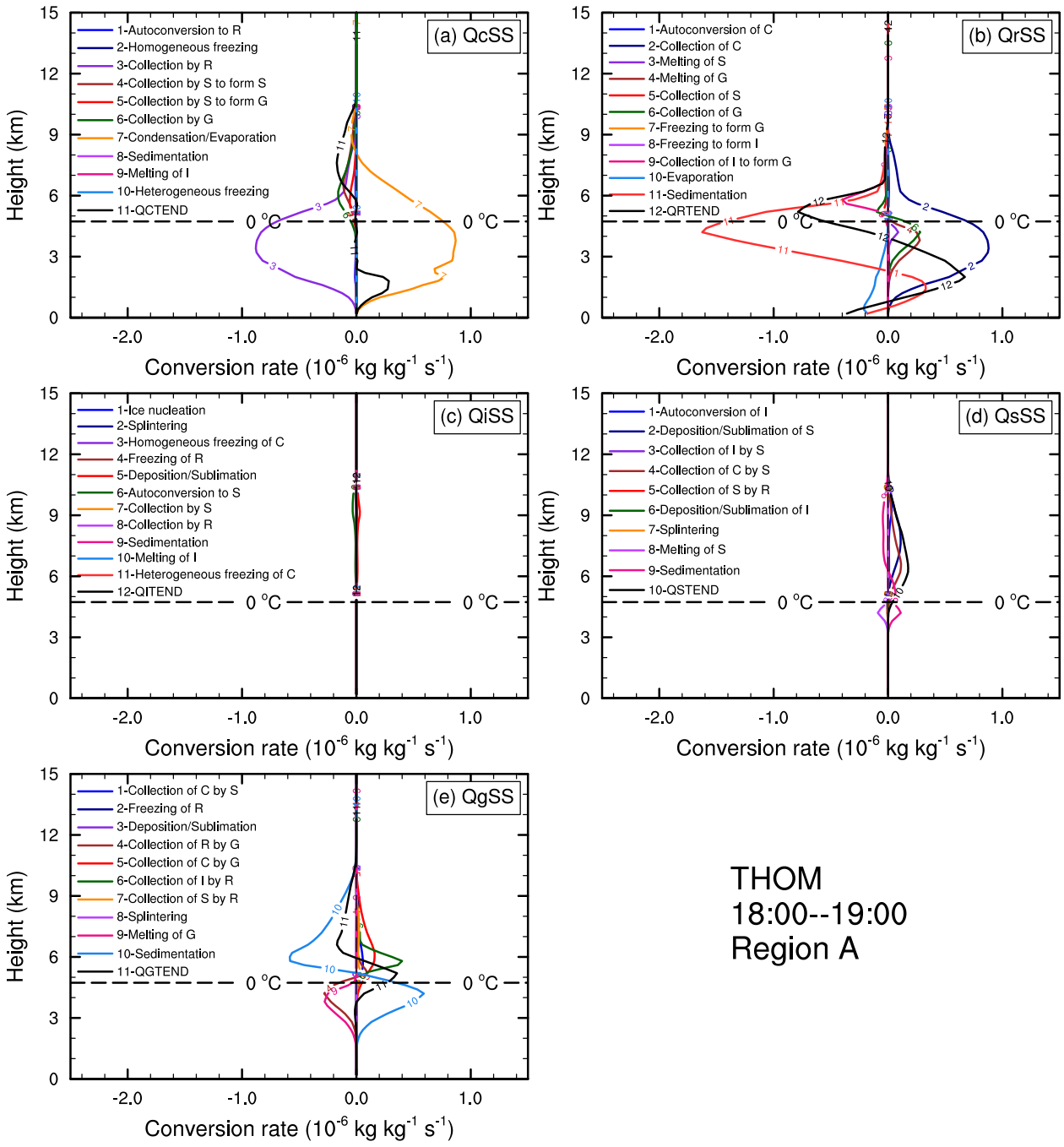

Fig. 8. As in Fig. 7, but for the THOM run.

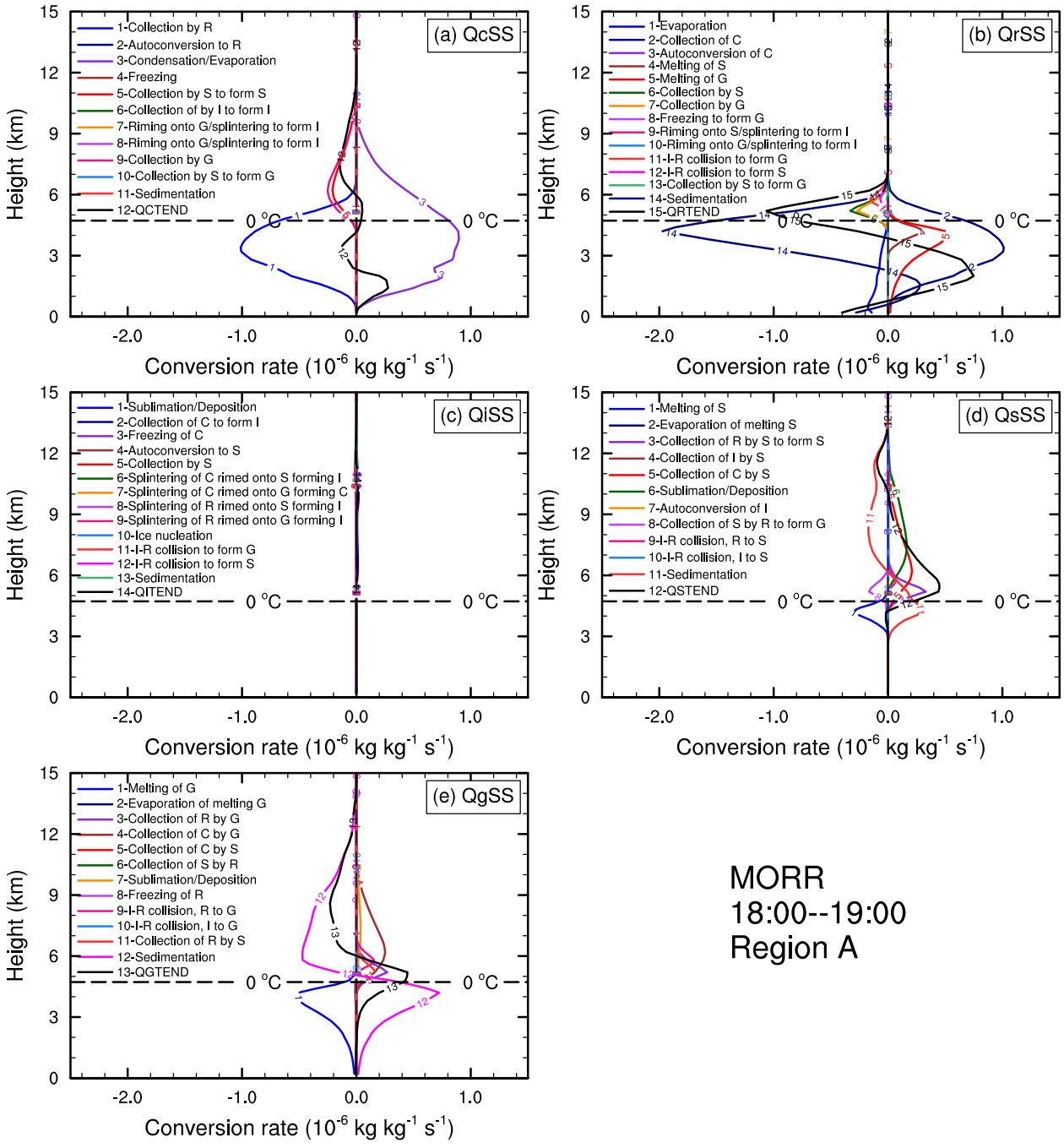

Fig. 9. As in Fig. 7, but for the MORR run.

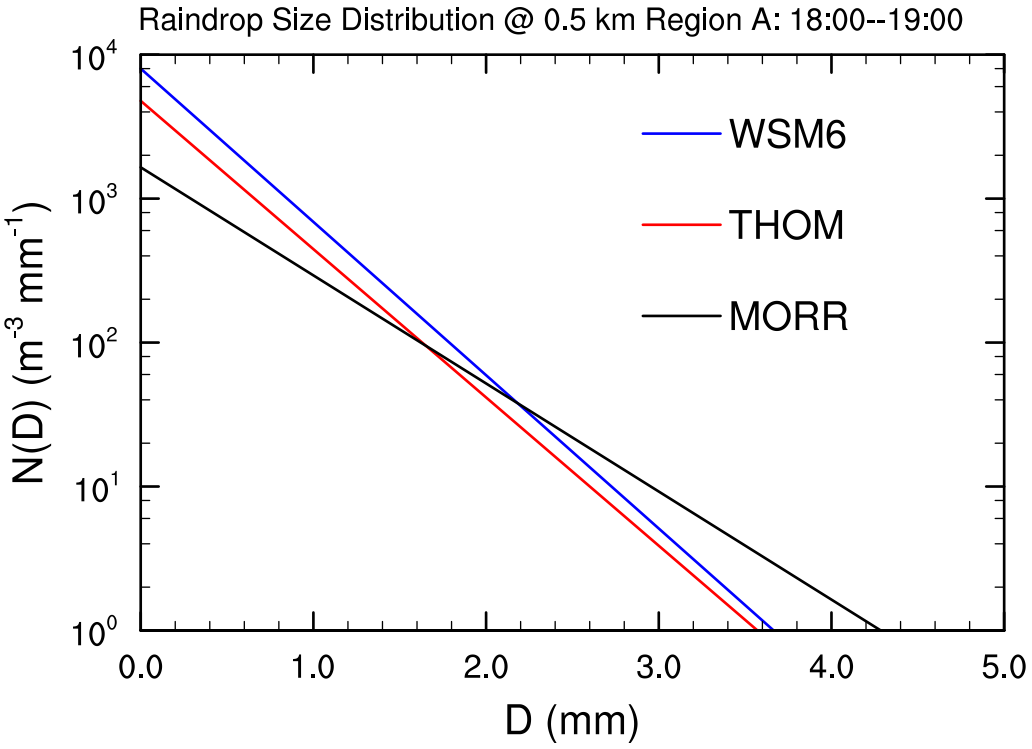

675

676 **Fig. 10.** Raindrop size distribution at 0.5 km in Region A during 1800–1900 UTC 06 May 2017

677 in the WSM6 (blue), THOM (red) and MORR (black) runs.

678

679

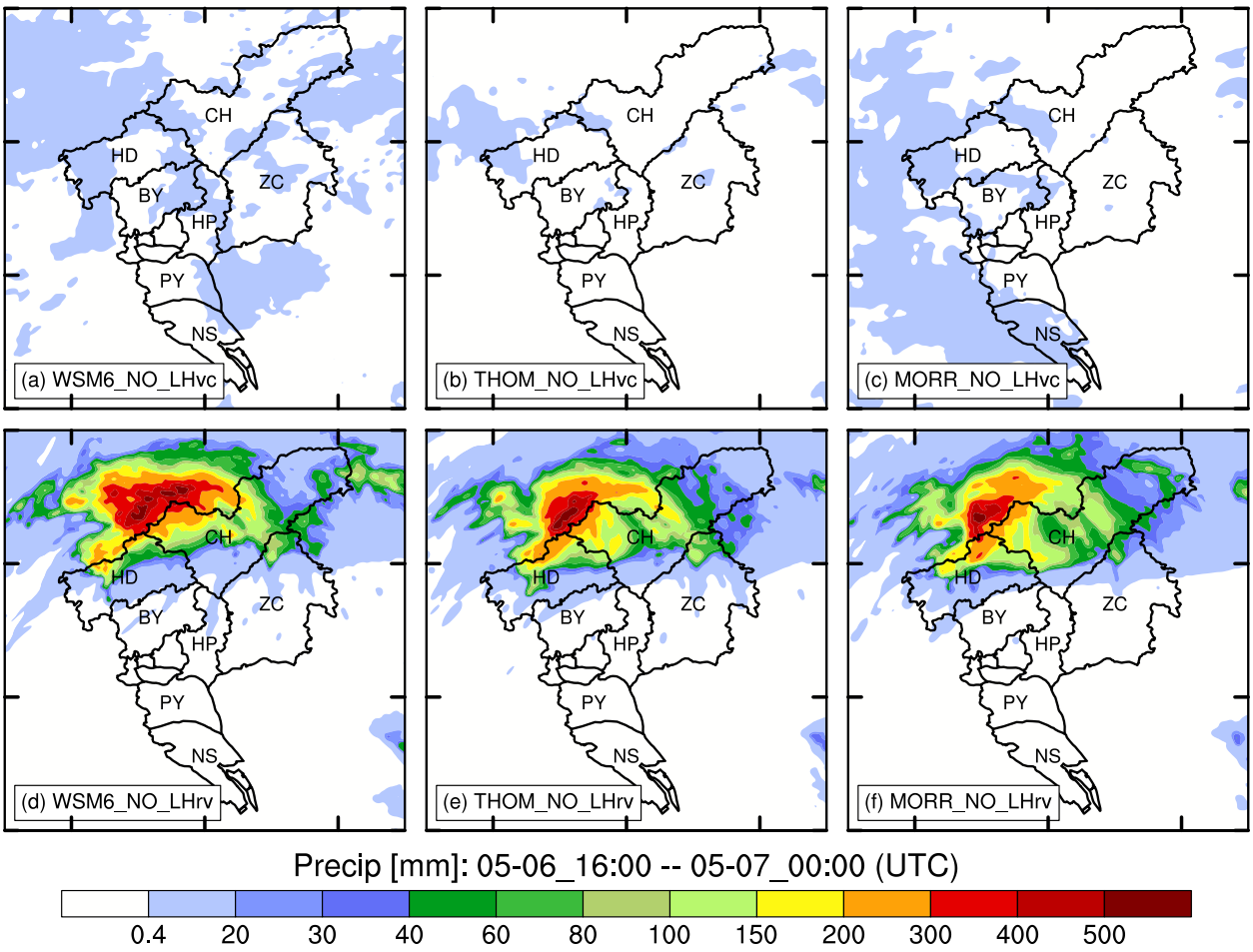

680

681 **Fig. 11.** Accumulated precipitation (mm) in the 0.5-km domain of (a, d) WSM6 run, (b, e) THOM
682 run and (c, f) MORR run after turning off latent heat due to (a–c) water vapor condensation to
683 form cloud water and (d–f) rain water evaporation in the Guangzhou region from 1600 UTC 06
684 May to 0000 UTC 07 May 2017. The black solid lines represent Guangzhou City and its district
685 borders. The initials are the same as those in Fig. 1. Tick marks are included every 50 km.